Journal of Solid State Electrochemistry (2023) 27:271–280
https://doi.org/10.1007/s10008-022-05319-3

ORIGINAL PAPER

# Electrical conductivity and electrochemical studies of Cr-doped $MoO_3$ nanoflakes for energy storage applications

R. Biju Bennie[1] · C. Joel[1] · A. Nirmal Paul Raj[1] · A. Jerold Antony[2] · S. Iyyam Pillai[3]

Received: 24 September 2022 / Revised: 19 October 2022 / Accepted: 23 October 2022 / Published online: 4 November 2022


## Abstract

The growing demand for electricity has increased the interest of the researchers towards exploration of energy storing devices (ESDs). With the motif for developing electrochemical energy storage devices, this research work is focussed on the study of $MoO_3$ nanoparticles and its doping with chromium as an efficient electrode material for energy storage applications. The nanoparticles were synthesized by hydrothermal method and were examined by powder X-ray diffraction, which determined the thermodynamically stable orthorhombic phase of $MoO_3$, and their morphologies were examined using scanning electron microscopy displaying flake-like structures. The typical vibrational bands of Mo–O were identified from Infra-red and Raman spectral analysis. The ultra violet diffuse reflectance spectra revealed the decrease in optical band gap after doping with chromium. The temperature dependent AC and DC conductivities were enhanced on doping. Electrochemical behaviour of the nanoparticles was probed by cyclic voltammetry (CV), electrochemical impedance spectroscopy (EIS) measurements and galvanostatic charge–discharge (GCD) analysis for which specific capacitance ($C_{sp}$) value of 334 $Fg^{-1}$ was achieved for Cr-doped $MoO_3$ nanoparticles. The electrochemical performance of the sample was found to be increased after doping with Cr.

**Keywords** $MoO_3$ · Cr doping · Electrical conductivity · Specific capacitance · GCD

## Introduction

The energy demand of the world is exponentially increasing with population rise. If surplus power is produced, the storage is always hasslesome. According to international energy agency (IEA), the COVID-19 pandemic is found to impact on global energy demand due to lockdowns, but it may increase due to massive vaccination and rescind of shutdown throughout the world citing the decrease in infection rate. In post pandemic period, it is envisaged that energy demand may increase by more than 4% in successive years [1]. The electricity demand is predicted to grow in a fast pace than in a decade over 1000 TWH [2]. In that context, energy storing devices (ESDs) are proved to be a bounty for the researchers, industrialists and the governments [3]. The ESDs are broadly classified into batteries and supercapacitors. Both the types have similar configurations that of electrochemical devices [4]. Among various renewable energy resources and storage systems, the research is burgeoning on these ESDs [5]. Notably, the uninterrupted energy supply being demanded by the consumers has its own impact on sustainability of environment to a greater extent [6].

Metal oxide nanoparticles are found to have versatile applications in electronics, spintronics, electronics, photo electronics, optoelectronics, laser technology, photocatalysis, sensors etc. [7]. Thus, the metal oxide nanoparticles are found as suitable candidates to be used in ESDs [8]. The electrically insulating pseudocapacitive properties of transition metal oxides in batteries and capacitors are found to be enhanced as the size of the material is reduced [9]. As the dimensions of energy storage materials were reduced in size, the diffusion path lengths of ions were decreased, thereby enhancing the non-insertion charge storage dramatically [10]. Metal oxides are being explored widely as anode materials for their striking electrochemical features. They are found to possess intercalation mechanism similar to that of graphite [11]. The performance of metal oxide is

✉ C. Joel
joeldcc@yahoo.co.in

[1] Postgraduate Department of Chemistry, St. John's College, Tirunelveli 627002 Tamil Nadu, India

[2] Department of Chemistry, St. Xavier's College (Autonomous), Tirunelveli 627002 Tamil Nadu, India

[3] Department of Chemistry, Pachaiyappa's College, Chennai 600030 Tamil Nadu, India

based on its morphology, size which in turn determines the diffusion kinetics and cyclability [12]. The wide band gap energy (presage as semiconductors) has not denied its role as electrodes or electrochemical sensors in energy devices.

Among different metal oxides with layered structures, $\alpha$-$MoO_3$ have gained distinct attention due to their unique properties such as high-specific surface area, chemical and photochemical stability, optical transparency and their ease of fabrication [13]. $MoO_3$ nanoparticles are broadly classified as three types, thermodynamically stable $\alpha$-$MoO_3$, metastable β-$MoO_3$ which can be reconverted to 'α' form by heating it above 400 °C and third form h-$MoO_3$ is a *n*-type semiconductor with band gap energy of 3.2 eV, with extraordinary photochromic and electrochromic properties [14]. $\alpha$-$MoO_3$ is considered to be one of the most promising low-cost material having high electrochemical activity and eco-friendly nature when compared with other transition metal oxides [15]. There are certain reports that emphasise the better electrochemical behaviour of $MoO_3$ nanoparticles [16–18], and also the enhancement in electrochemical behaviour of certain metal oxides when doped with chromium [19, 20]. Cr as Cr(III)/Cr(II) is used as an anode in redox energy storage system with Fe(III)/Fe(II) as counter electrode. This triggered us to carry out the electrochemical studies for $MoO_3$ on doping with Cr since it has been not reported yet and is considered to be the novelty of the present work.

In the present work, chromium is used as dopant for enhancing the energy storage properties of the $MoO_3$ nanoparticles. Doping of chromium has proved to exhibit a synergic effect on electrochemical properties which is greatly attributed to bulk doping, surface coating and reduction in size [21]. It is also corroborated that dopant chromium improves discharge capacity and columbic efficiency of electrode materials, and hence it is considered as a suitable candidate for doping in our study.

## Methods and materials

### Preparation of undoped and chromium-doped $MoO_3$ NPs

To synthesise $MoO_3$ nanoparticles, accurately weighed 0.1 M ammonium heptamolybdate tetrahydrate (AHM) $(NH_4)_6Mo_7O_{24}{\cdot}4H_2O$) was dissolved in 50 mL of deionised water and stirred constantly for 20 min at room temperature. To this solution, hydrochloric acid (1 M) was added dropwise to form molybdic acid at pH ~ 1 and stirring was continued for 4 h to obtain white precipitate. This precipitate was then washed recurrently with deionised water and ethanol until free from impurities, filtered using whatman filter paper and then dried in hot air oven for 6 h at 60 °C. The product was finally annealed at 400 °C for 2 h in a muffle furnace to get $MoO_3$ nanoparticles. Similar procedure was implemented for the synthesis of Cr-doped $MoO_3$. During the reaction course, chromium (III) nitrate nonahydrate (0.1215 g, 0.5 mmol) was added along with AHM.

### Instrumentation techniques

The powder XRD of all the samples were analysed on X'pert PRO model powder X-ray diffractometer in $2\theta$ range of 20°–60° obtained at a scan rate of 2° $min^{-1}$ involving the source of Cu-$K_\alpha$ X-ray radiation. The morphologies of the sample surface were imaged using JSM-6700 model field emission scanning electron microscope (JEOL, Japan) for which the elemental compositions were achieved on Quan-Tax 200 Energy Dispersive X-ray spectrometer (RONTEC's EDX system, Germany). The HRTEM images were scanned using JEM-2100 Plus model high-resolution transmission electron microscope of JEOL, Japan. The FTIR spectra were recorded on SHIMADZU spectrometer by pelletizing the samples with KBr in the range of 4000–400 $cm^{-1}$. FT Raman spectra of the samples were recorded by exciting the samples at a wavelength of 1064 nm using the source Nd:YAG laser on EZ Raman IFS 66 V spectrometer of Enwave optronics, made in the USA. DRS coupled JASCO V-530 dual beam spectrophotometer was equipped for recording the absorption spectra. The frequency-dependent conductivity measurements of all the samples were performed by Precision LCR Meter (Agilent 4284A) covering the frequency range from 100 Hz to 1 MHz, within a temperature range of 303 to 383 K. Each of the samples was positioned between a pair of blocking electrodes having a diameter of 2.5 cm under spring pressure. Electrochemical investigations of the samples were performed on a three-electrode system, taking the synthesized nanoparticles working electrodes, Ag/AgCl as reference electrode and platinum wire as the counter electrode.

### Electrode fabrication

The slurry of electrode material was prepared from 85 wt% of synthesized nanoparticles, 10 wt% of activated carbon (Sigma-Aldrich) and 5 wt% of polytetrafluoroethylene (Sigma-Aldrich) using ethanol. The working electrode was prepared by a thin coating of this slurry onto a nickel foil (1 $cm^2$) and drying at 80 °C for 8 h. All the electrochemical analyses were performed at room temperature taking 2 M KOH as electrolytic solution. The specific capacitance ($C_{sp}$), energy density ($E$), and power density ($P$) values were calculated from the obtained GCD curves using the following relations [22]:

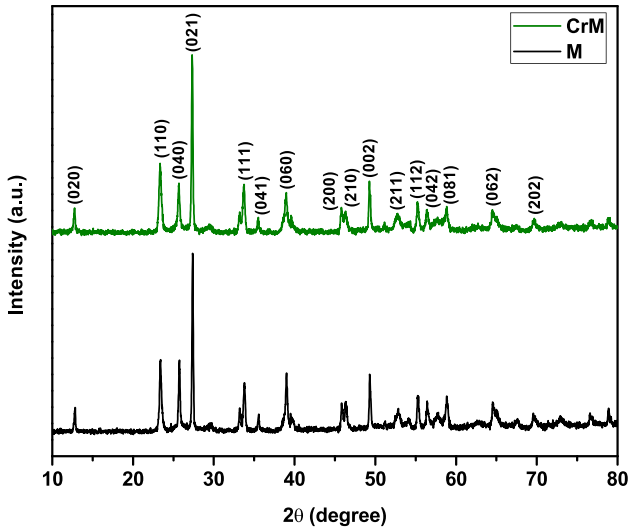


**Fig. 1** XRD patterns of $MoO_3$ and Cr-doped $MoO_3$ NPs

$$C_{sp} = \frac{I_d \times T_d}{\Delta V \times m}$$

$$E = \frac{1}{2} C_{sp} (\Delta V)^2$$

$$P = \frac{E \times 3600}{T_d}$$

where $I_d$ and $T_d$ = discharge-current and discharge time, $m$ = loaded mass of electrode, $\Delta V$ = potential window.

## Results and discussion

The structure and phase purity of the synthesized $MoO_3$ and Cr-doped $MoO_3$ NPs were analysed by X-ray diffraction analysis. The peaks (Fig. 1) could be well indexed to the orthorhombic phase of $MoO_3$ in accordance to the reported literature values (JCPDS card No. 05–0508) [23]. The space group and the lattice parameters were found to be P*bnm* and $a = 3.962$ Å, $b = 13.858$ Å and $c = 3.697$ Å respectively [24]. The lattice parameter values of doped sample were found to be $a = 3.973$ Å, $b = 13.749$ Å and $c = 3.583$ Å. The high intense peaks at 23.35°, 25.67° and 27.33° corresponds to (1 1 0), (0 4 0) and (0 2 1) planes showing the better crystalline nature of the NPs.

Due to low Cr concentration and also the radius of $Mo^{6+}$ (0.59 A°) nearly same as that of $Cr^{3+}$ (0.62 A°), no change in XRD peaks were observed after doping. But the change in lattice parameter values confirms the effective doping of $Cr^{3+}$ into the lattices of $MoO_3$.

The morphologies of the NPs were observed from scanning electron microscopic images at various magnifications (Fig. 2(a–h)) which were found to exist as flakes. The incorporation of Cr ions in $MoO_3$ did not affect the morphology for doped sample. The energy dispersive X-ray spectroscopy analysis also confirmed that no other impurities were detected from the elemental composition of $MoO_3$ and Cr-doped $MoO_3$. The high intensity peaks arising at 2.3 keV and 0.5 keV corresponds to Mo and O atoms respectively present in the $MoO_3$ nanoparticles. Elemental mappings (Fig. 3) of the prepared samples revealed

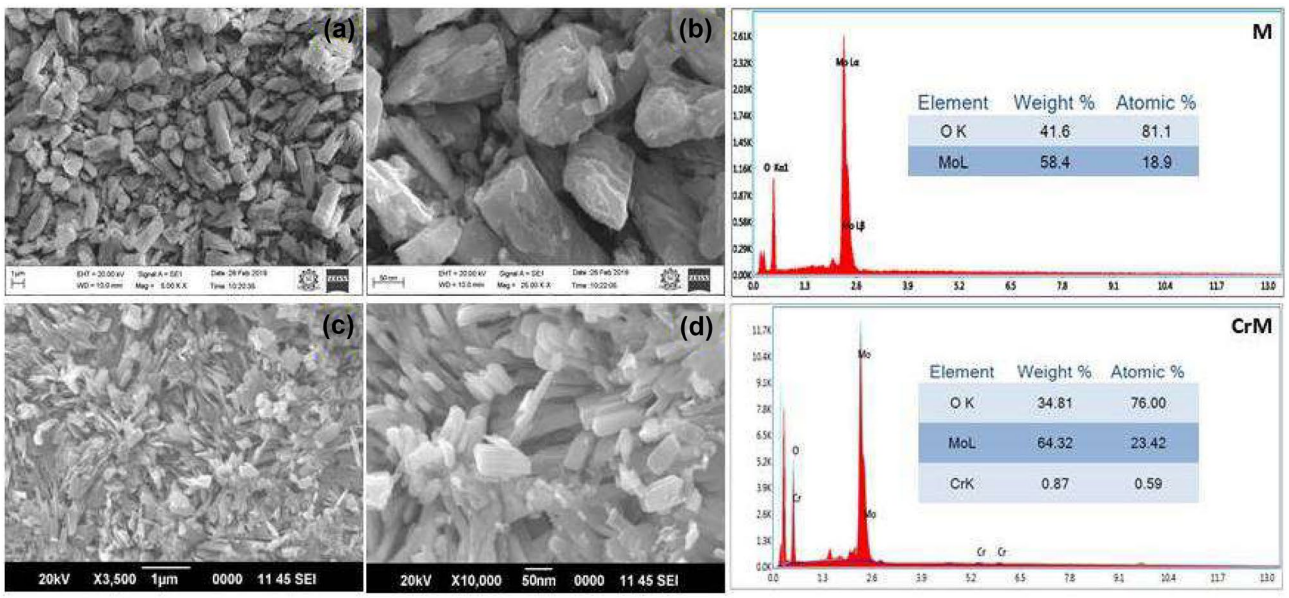


**Fig. 2** SEM images and EDX spectra of $MoO_3$ (**a**, **c**) and Cr-doped $MoO_3$ (**b**, **d**) NPs

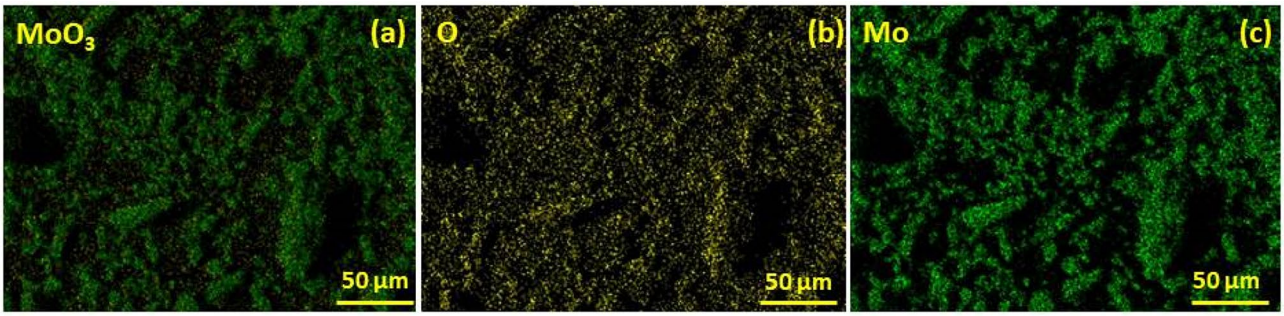


a Elemental mapping of $MoO_3$ NPs

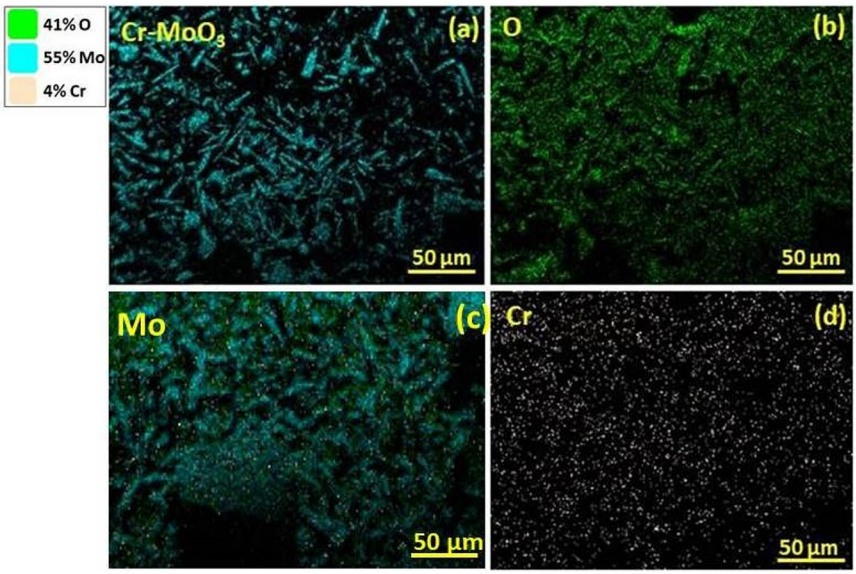


b Elemental mapping of Cr doped $MoO_3$ NPs

**Fig. 3** (**a**) Elemental mapping of $MoO_3$ NPs. (**b**) Elemental mapping of Cr -doped $MoO_3$ NPs

the presence of Cr, Mo and O atoms. Moreover, the mapping of elements exposed that both the undoped and doped nanoparticles were homogenously distributed. The TEM and HRTEM images of $MoO_3$ and Cr-doped $MoO_3$ nanoparticles (Fig. 4a–d) exhibits observable lattice fringes of crystallographic planes whose *d* spacing were found to be 0.326 nm and 0.324 nm for $MoO_3$ and Cr-doped $MoO_3$ respectively corresponding to (021) plane.

Figure 5 shows the vibrational spectra of the NPs in which the bands observed at 2335, 2976 and 3222 $cm^{-1}$ seem to arise from the H–O–H bending mode and symmetric and asymmetric O–H modes for the water of representation [25]. The strong vibration bands observed at 972 $cm^{-1}$, 868 $cm^{-1}$ corresponds to the stretching vibrations of Mo = O [26]. The less intense peak at 635 $cm^{-1}$ and sharp peak at 506 $cm^{-1}$ indicate the stretching vibrations of oxygen atoms in Mo–O–Mo units and vibrations of oxygen atoms linked to three molybdenum atoms, respectively [27].

The Raman spectra (Fig. 6) shows a well-defined sharp peak at 1004 $cm^{-1}$ representing the asymmetric stretching vibrations of the terminal $Mo^{6+} = O$ bonds [28]. The high intensity peak observed at 823 $cm^{-1}$ could be ascribed to the symmetric stretching of Mo–O-Mo bonds [29]. The broad band observed at 663 $cm^{-1}$ corresponds to the asymmetric stretching and the weak band at 460 $cm^{-1}$ is attributed to bending vibrations of triply coordinated oxygen Mo–O-Mo bonds. Moreover, the band seen at 364 $cm^{-1}$ can be assigned to the scissoring mode of O–Mo-O bonds [30]. The band centred at 326 $cm^{-1}$ originates from the bending vibrations of O–Mo-O bonds. The characteristic band at 272 $cm^{-1}$ is ascribed to the Mo = O wagging modes of the terminal oxygen atom [31]. The samples doped with Cr showed the same Raman peaks as the pure α-$MoO_3$ sample (Fig. 4a), indicating that the crystalline structure was preserved during the doping process [32].

The UV–Vis absorption spectra of the samples are shown in Fig. 7, $\alpha$-$MoO_3$ exhibit an absorption onset at

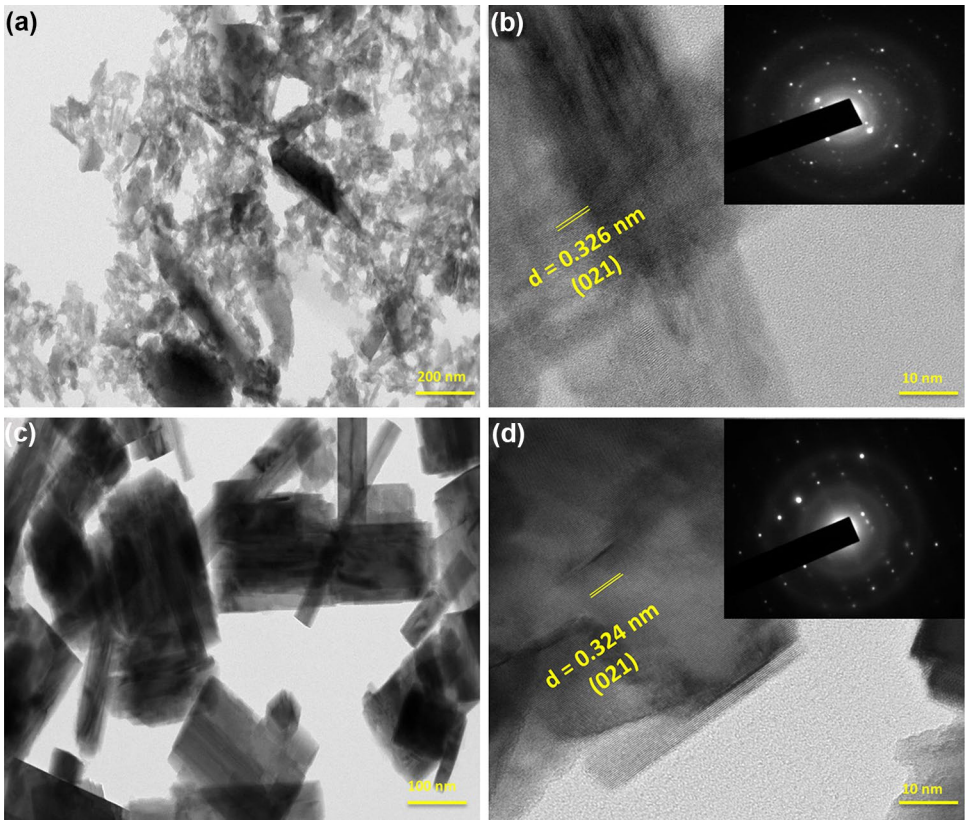


**Fig. 4** TEM images (**a**, **b**) and HRTEM images (**c**, **d**) (inset: SAED pattern) of $MoO_3$ and Cr-doped $MoO_3$ NPs

432 nm and 465 nm for Cr-doped nanoparticles. The direct band gap energies of both undoped and doped nanoparticles are calculated using Kubelka–Munk (K–M) function as follows [33]:

$$F(R) = \frac{(1-R)^2}{2R} = \frac{K(\lambda)}{S(\lambda)} \infty \alpha = \frac{(h\upsilon - E_g)^n}{h\upsilon}$$

where $R$ denotes the diffuse reflectance of the samples. Here, the direct band gap can be obtained by drawing a tangent on the curve obtained on plotting $(F(R)h\upsilon)^2$ vs. photon energy ($h\upsilon$). The band gap energies of M and CrM were calculated to be 2.83 eV and 2.64 eV respectively.

Electrical conductivity of a semiconductor is a temperature dependent process that occurs due to orderly motion of weakly held charged particles under the effect of an applied

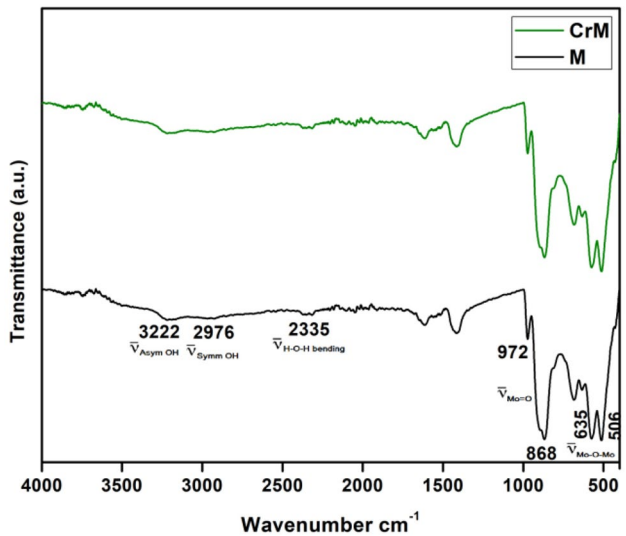


**Fig. 5** FTIR spectra of $MoO_3$ and Cr-doped $MoO_3$ NPs

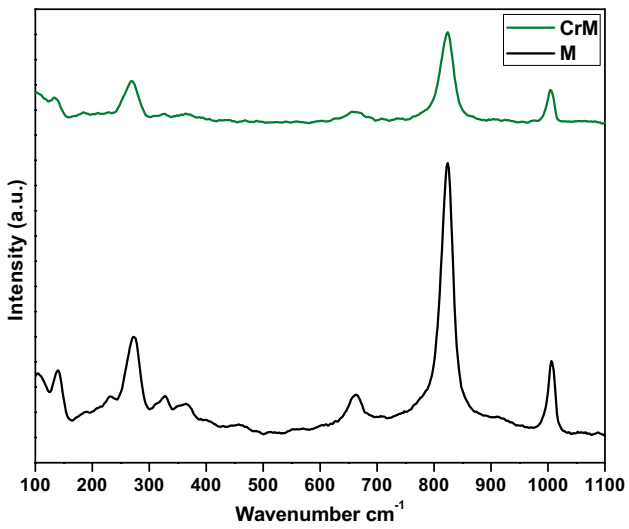


**Fig. 6** Raman spectra of $MoO_3$ and Cr-doped $MoO_3$ NPs

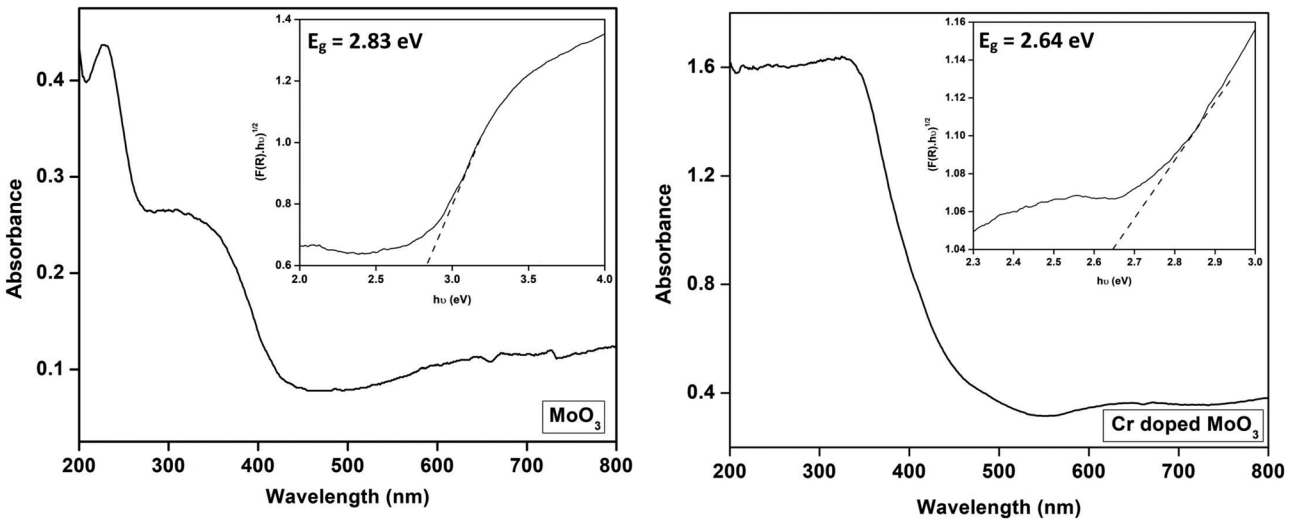


**Fig. 7** Absorbance spectra of $MoO_3$ and Cr-doped $MoO_3$ NPs (inset: band gap calculation using Kubelka–Munk (K–M) function for $MoO_3$ and Cr-doped $MoO_3$ nanoparticles)

electric field. The frequency-dependent ac conductivity ($\sigma_{ac}$) was calculated using the following formula [34]:

$$\sigma_{ac}(\omega) = G_p(\omega) \cdot \frac{t}{A}$$

where $G_p$ is the measured conductance of the sample, $t$ and $A$ are the thickness of the sample and contact area between the electrode and electrolytic surface respectively. The AC conductivity of the undoped and Cr-doped $MoO_3$ samples at varying temperatures are shown in Fig. 8. From the figure, two points are considered: (i) a plateau at low frequency region which is related to DC conductivity ($\sigma_{dc}$), (ii) the high frequency corresponds to a bulk relaxation phenomenon, which arises on account of migration of trapped ions related to ac conductivity [35]. It is observed that the $\sigma_{ac}$ values for all the samples increases on raising the frequency and also temperature, showing that the most probable mechanism for conductivity of $MoO_3$ and Cr-doped $MoO_3$ nanoparticles is ion hopping mechanism [36]. It is also observed from the figure that AC conductivity increases on Cr-doping due to the induced charge carrier density by the addition of dopant [37].

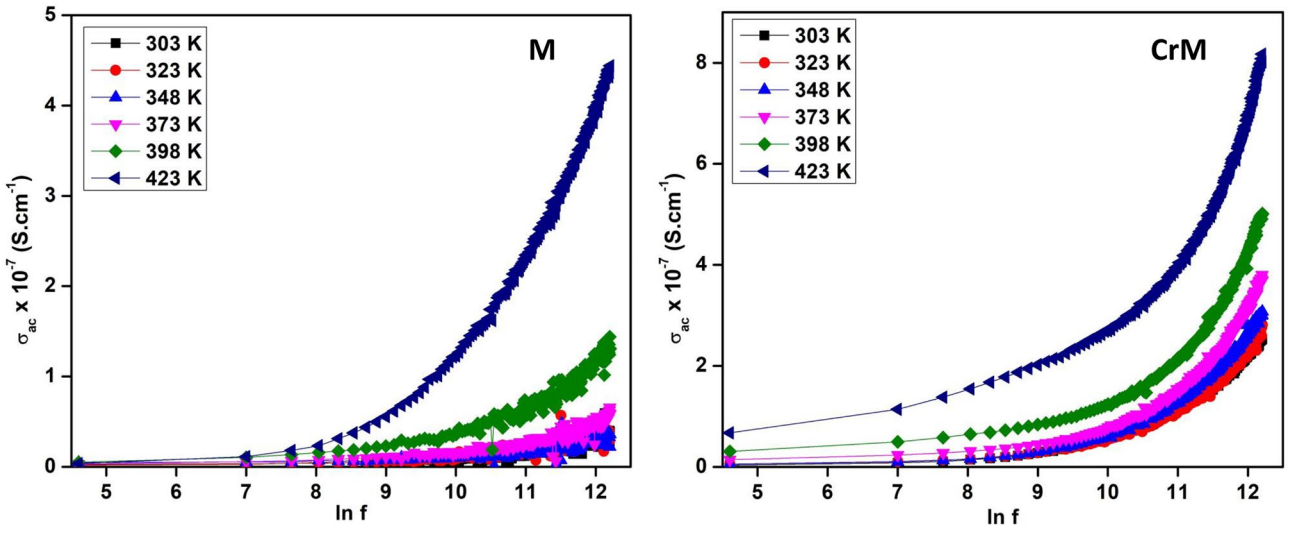


**Fig. 8** Frequency-dependent $\sigma_{ac}$ of $MoO_3$ and Cr-doped $MoO_3$ NPs at varying temperatures

**Table 1** The values of $\sigma_{dc}$, $S$ and $E_a$ for $MoO_3$ and Cr-doped $MoO_3$ NPs

| Compound | $T$ (K) | $\sigma_{dc} \times 10^{-9}$ (S.cm$^{-1}$) |
|---|---|---|
| $MoO_3$ | 303 | 4.09 |
| | 323 | 4.78 |
| | 348 | 5.18 |
| | 373 | 6.82 |
| | 398 | 8.03 |
| | 423 | 8.33 |
| Cr-doped $MoO_3$ | 303 | 5.62 |
| | 323 | 6.64 |
| | 348 | 7.31 |
| | 373 | 11.94 |
| | 398 | 15.53 |
| | 423 | 19.32 |

The DC conductivity ($\sigma_{dc}$) arises due to hopping of metal ions in a random manner between the defects states [38]. The $\sigma_{dc}$ values (Table 1) are obtained by extrapolating the plateau of the $\sigma_{ac}$ spectra in Fig. 7. The temperature dependent $\sigma_{dc}$ increases after doping due to the availability of Cr ions for migration.

The electrochemical performance of M and CrM were studied by cyclic voltammetry (CV). The redox peaks observed in both the samples (Fig. 9) indicate the charges which could be associated to faradic redox reactions [39].

The doped sample showed greater current response when compared to that of undoped electrode. For undoped sample, the oxidation peak was observed at 0.4 V (11 A/g) and reduction peak at 0.2 V (− 8 A/g) was obtained for undoped sample while for doped sample, the oxidation peak was found at 0.4 V (19 A/g) and reduction peak at 0.2 V (− 12 A/g). This confirms that the doped sample having interconnected network possess good porosity, thereby leading to better mobilization of electrons from electrolyte to the electrode surface [40].

The GCD analysis is considered as the more sensible approach to better understand the supercapacitive features present in a material [41]. The GCD profiles are recorded in the potential range of 0–0.5 V at different current densities from 1 to 10 A/g and are presented in Fig. 10.

The specific capacitance values along with energy and power density values for $MoO_3$ and Cr-doped $MoO_3$ nanoparticles are provided in Table 2.

The electrodes M and CrM have specific capacitance values of 230 and 344 F g$^{-1}$ at the current density of 1 Ag$^{-1}$. The specific capacitance values decreases at higher scan rates due to the existence of inner active sites which is unable to withstand the redox transition. The small convexer appearing in GCD curves is attributed to the doping of Cr ions and its participation in redox reactions. The minor voltage drop observed during discharging is an indicative of the conducting nature of the electrodes. Furthermore, the discharge time was decreased as current densities increased from 1 to 10 Ag$^{-1}$ which was also the same trend for specific capacitance values. It could be attributed to less ion diffusion in electrolyte and charge transfer in the electrode material resulting in less active material's participation in redox reactions and thus increase in the polarization value at higher current densities [42].

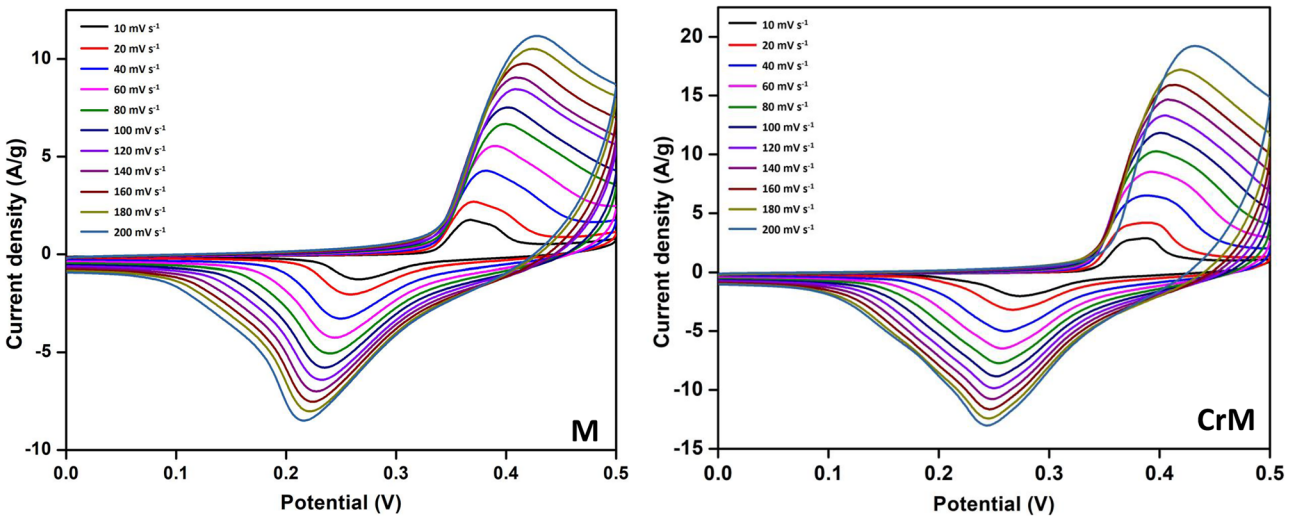


**Fig. 9** CV curves of $MoO_3$ and Cr-doped $MoO_3$ NPs at various scan rates

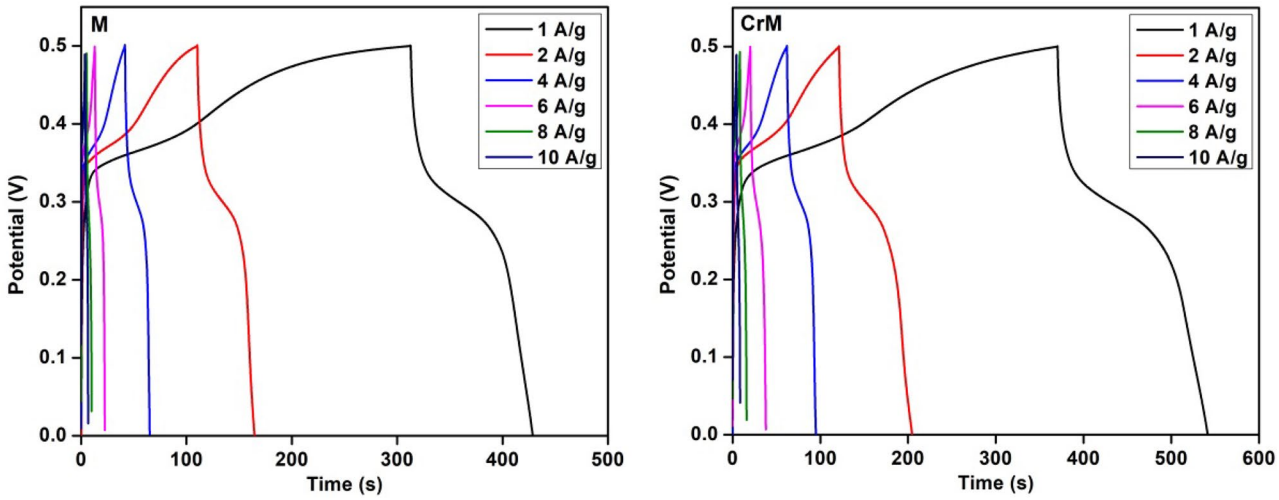


**Fig. 10** GCD curves of $MoO_3$ and Cr-doped $MoO_3$ NPs with various applied current

**Table 2** Specific capacitance ($C_{sp}$) values of synthesized NPs

| Current density (A/g) | Specific capacitance (F/g) | | Energy density (W h $Kg^{-1}$) | | Power density (W $Kg^{-1}$) | |
|---|---|---|---|---|---|---|
| | M | CrM | M | CrM | M | CrM |
| 1 | 230 | 344 | 28 | 43 | 900 | 900 |
| 2 | 216 | 336 | 27 | 42 | 1800 | 1800 |
| 4 | 192 | 264 | 24 | 33 | 3600 | 3600 |
| 6 | 108 | 216 | 13 | 27 | 5400 | 5400 |
| 8 | 80 | 128 | 10 | 16 | 7200 | 7200 |
| 10 | 60 | 80 | 7 | 10 | 9000 | 9000 |

## Conclusion

The $MoO_3$ and Cr-doped $MoO_3$ nanomaterials were prepared via hydrothermal route. The powder XRD analyses could be indexed to thermodynamically stable orthorhombic phase with space group *Pbnm*. The SEM and HRTEM revealed the flake-like morphologies. The direct band gap energies obtained using Kubelka–Munk relation shows a decrease in band gap value after doping. The AC conductivity revealed that the mechanism behind conduction process is ion hopping. The DC conductivity increases after doping due to the migration of Cr ions. From CV studies, the doped sample shows better redox behaviour due to the interconnected network leading to ion mobilization. The specific capacitance of $MoO_3$ was increased after doping with chromium at the current density of 1 $Ag^{-1}$ making it a promising material for energy storage applications.

**Acknowledgements** The authors thank the Department of Physics, St. John's College, Tirunelveli for the conductivity studies. Also We would like to thank Dr. B. Saravanakumar, Materials Research Laboratory, Dr. Mahalingam College of Engineering and Technology, Pollachi, for the electrochemical analysis.

**Author contribution** R. Biju Bennie. A: conceptualization, methodology, formal analysis, investigation, writing—original draft, writing review and editing. A. Nirmal Paul Raj: validation, formal analysis, resources, writing review and editing, visualisation. A. Jerold Antony: methodology, resources, data curation, writing—original draft, writing review and editing. S. Iyyam Pillai: methodology, formal analysis, investigation, resources. C. Joel: conceptualization, supervision, project administration.

**Data availability** All data generated or analysed during this study are included in this published article.

## Declarations

**Conflict of interest** The authors declare no competing interests.

## References

1. Jiang P, Fan YV, Klemeš JJ (2021) Impacts of COVID-19 on energy demand and consumption: challenges, lessons and emerging opportunities. Appl Energy 285:116441
2. Asif M, Muneer T (2007) Energy supply, its demand and security issues for developed and emerging economies. Renew Sustain Energy Rev 11(7):1388–1413

3. Andonia M, Robu V, Flynn D, Abram S, Geach D, Jenkins D, McCallum P, Peacock A (2019) Blockchain technology in the energy sector: a systematic review of challenges and opportunities. Renew Sustain Energy Rev 100:143–174
4. Guoab B, Liang G, Yua S, Wang Y, Zhi C, Bai J (2021) 3D printing of reduced graphene oxide aerogels for energy storage devices: a paradigm from materials and technologies to applications. Energy Storage Mater 39:146–165
5. Gerard O, Numan A, Krishnan S, Khalid M, Subramaniam R, Kasi R (2022) A review on the recent advances in binder-free electrodes for electrochemical energy storage application. J Energy Storage 50:104283
6. Noor S, Yang W, Guo M, Van Dam KH, Wang X (2018) Energy demand side management within micro-grid networks enhanced by blockchain. Appl Energy 228:1385–1398
7. Lu JG, Chang P, Fan Z (2006) Quasi-one-dimensional metal oxide materials—synthesis, properties and applications. Mater Sci Eng R Rep 52(1–3):49–91
8. Wang R, Li X, Nie Z, Zhao Y, Wang H (2021) Metal/metal oxide nanoparticles-composited porous carbon for high-performance supercapacitors. J Energy Storage 38:102479
9. Low WH, Khiew PS, Lim SS, Siong CW, Ezeigwe ER (2019) Recent development of mixed transition metal oxide and graphene/mixed transition metal oxide based hybrid nanostructures for advanced supercapacitors. J Alloys Compd 775:1324–1356
10. Arani MG, Niasari MS (2022) Comparative study on electrochemical hydrogen storage of nanocomposites based on S or N doped graphene quantum dots and nanostructured titanium niobate. J Alloys Compd 899:163379
11. Qin J, Sari HMK, Wang X, Yang H, Zhang J, Li X (2020) Controlled design of metal oxide-based ($Mn^{2+}$/$Nb^{5+}$) anodes for superior sodium-ion hybrid supercapacitors: synergistic mechanisms of hybrid ion storage. Nano Energy 71:104594
12. Ellis BL, Knauth P, Djenizian T (2014) Three-dimensional self-supported metal oxides for advanced energy storage. Adv Mater 26(21):3368–3397
13. Zhou J, Xu NS, Deng SZ, Cheng J, She JC, Wang ZL (2003) Large-area nanowire arrays of molybdenum and molybdenum oxides: synthesis and field emission properties. Adv Mater 15(21):1835–1840
14. Nagarajua P, Arivanandhan M, Alsalme A, Alghamdi A, Jayavel R (2020) Enhanced electrochemical performance of α-$MoO_3$/graphene nanocomposites prepared by an in situ microwave irradiation technique for energy storage applications. RSC Adv 10(38):22836–22847
15. Shakir I, Shahid M, Yang HW, Kang DJ (2010) Structural and electrochemical characterization of -$MoO_3$ nanorod-based electrochemical energy storage devices. Electrochimi Acta 56(1):376–380
16. Deokate RJ, Kate R, Shinde NM, Mane RS (2021) Energy storage potential of sprayed α-$MoO_3$ thin films. New J Chem 45(2):582–589
17. Yu M, Shao H, Wang G, Yang F, Liang C, Rozier P, Wang CZ, Lu X, Simon P, Feng X (2020) Interlayer gap widened α-phase molybdenum trioxide as high-rate anodes for dual-ion-intercalation energy storage devices. Nat Commun 11:1348
18. Shakir I, Shahid M, Woo H, Dae Y, Kang J (2010) Structural and electrochemical characterization of α-$MoO_3$ nanorod-based electrochemical energy storage devices. Electrochim Acta 56(1):376–380
19. Ahmed R, Nabi G (2021) Enhanced Electrochemical Performance of Cr-doped NiO nanorods for supercapacitor application. J Energy Storage 33:102115
20. Moussa NM, Ebrahim FM, Adly K, Hassaan MY (2022) Chromium doped ZnO nanoparticles for energy storage, gas and humidity sensing and spin based electronic devices applications. Opt Quant Electron 54:683
21. Zou H, Liang X, Feng X, Xiang H (2016) Chromium-modified $Li_4Ti_5O_{12}$ with a synergistic effect of bulk doping, surface coating, and size reducing. ACS Appl Mater Interfaces 8(33):21407–21416
22. Munawar T, Rehman MN, Nadeem MS, Mukhtar F, Manzoor S, Ashiq MN, Iqbal F (2021) Facile synthesis of Cr-Co co-doped CdO nanowires for photocatalytic, antimicrobial, and supercapacitor applications. J Alloys Compd 885:160885
23. Bai S, Chen C, Tian Y, Chen S, Luo R, Li D, Liu CC (2015) Facile synthesis of α-$MoO_3$ nanorods with high sensitivity to CO and intrinsic sensing performance. Mater Res Bull 64:252–256
24. Wang S, Zhang Y, Ma X, Wang W, Li X, Zhang Z, Qian Y (2005) Hydrothermal route to single crystalline α-$MoO_3$ nanobelts and hierarchical structures. Solid state commun 136(5):283–287
25. Pradeesh G, Ponnuswamy V, Gowtham B, Suresh R, Chandrasekaran J (2018) Influence of annealing temperature on the properties of molybdenum oxide nanoparticles prepared through chemical precipitation method for p-n junction diode application. Optik 175:217–227
26. Sen SK, Dutta S, Khan M, Manir MS, Dutta S, Al Mortuza A, Hakim MA (2019) Characterization and antibacterial activity study of hydrothermally synthesized h-$MoO_3$ nanorods and α-$MoO_3$ nanoplates. Bio Nano Sci 9(4):873–882
27. Wongkrua P, Thongtem T, Thongtem S (2013) Synthesis of h-and α-$MoO_3$ by refluxing and calcination combination: phase and morphology transformation, photocatalysis, and photosensitization. J Nanomater 2013:1–8
28. Liu D, Lei WW, Hao J, Liu DD, Liu BB, Wang X, Chen XH, Cui QL, Zou GT, Liu J, Jiang S (2009) High-pressure Raman scattering and X-ray diffraction of phase transitions in $MoO_3$. J Appl Phys 105(2):023513
29. Farzi-kahkesh S, Rahmani MB, Fattah A (2020) Growth of novel α-$MoO_3$ hierarchical nanostructured thin films for ethanol sensing. Mater Sci Semicond Process 120:105263
30. Dieterle M, Weinberg G, Mestl G (2002) Structural characterization of oxygen defects in $MoO_{3-x}$ by DR UV/VIS, Raman spectroscopy and X-ray diffraction. Phys Chem Chem Phys 4(5):812–821
31. Silveira JV, Batista JA, Saraiva GD, Mendes Filho J, Souza Filho AG, Hu S, Wang X (2010) Temperature dependent behavior of single walled $MoO_3$ nanotubes: a Raman spectroscopy study. Vib. Spectrosc 54(2):179–183
32. Lima CD, Moura JV, Pinheiro GS, Araujo JF, Gusmão SB, Viana BC, Luz-Lima C (2021) Co-doped α-$MoO_3$ hierarchical microrods: Ssynthesis, structure and phonon properties. Ceram Int 47(19):27778–27788
33. Raj A, Adinaveen T, Bennie RB, Joel C, Kengaram SH, Sophie PL (2022) Nanoarchitectonics and electrochemical behavior of Cu doped h-$MoO_3$ as an electrode material for energy storage applications. J Inorg Organomet Polym Mater 1–11
34. Abdullah OG, Salman YAK, Saleem SA (2016) Electrical conductivity and dielectric characteristics of in situ prepared PVA/HgS nanocomposite films. J Mater Sci Mater Electron 27(4):3591–3598
35. Abdullah OG, Hanna RR, Ahmed HT, Mohamad AH, Saleem SA, Saeed MA (2021) Conductivity and dielectric properties of lithium-ion biopolymer blend electrolyte based film. Results Phys 24:104135
36. Qayoom M, Shah KA, Pandit AH, Firdous A, Dar GN (2020) Dielectric and electrical studies on iron oxide (α-$Fe_2O_3$) nanoparticles synthesized by modified solution combustion reaction for microwave applications. J Electroceram 45(1):7–14
37. Siddiqui H, Parra MR, Qureshi MS, Malik MM, Haque FZ (2018) Studies of structural, optical, and electrical properties associated with defects in sodium-doped copper oxide (CuO/Na) nanostructures. J Mater Sci 53(12):8826–8843

38. Atta AA, Wahba HH, Alkathiri AA, Waly AL, Al-hasni B, Ahmed EM (2022) On the electric and dielectric properties of some boro-lead sulphate glasses. Glass Phys Chem 48(3):187–201
39. Isacfranklin M, Yuvakkumar R, Ravi G, Velauthapillai D, Pannipara M, Al-Sehemi AG (2021) Superior supercapacitive performance of $Cu_2MnSnS_4$ asymmetric devices. Nanoscale Adv 3(2):486–498
40. Li P, Wang W, Su F, Wang X, Zhang X, Zheng X (2022) N-doped interconnected porous graphene as advanced electrode material for supercapacitors. J Alloys Compd 893:162218
41. Purkait T, Singh G, Kumar D, Singh M, Dey RS (2018) High-performance flexible supercapacitors based on electrochemically tailored three-dimensional reduced graphene oxide networks. Sci Rep 8(1):1–13
42. Ali F, Khalid NR (2020) Facile synthesis and properties of chromium-doped cobalt oxide (Cr-doped $Co_3O_4$) nanostructures for supercapacitor applications. Appl Nanosci 10(5):1481–1488